Turbulent Channel Flow Diagnostics by means of Shake-the-Box (STB): Flow Structures and Sublayer Profiles

J. Kriegseis[1,*], R. Leister[1], T. Rockstroh[2], R. Beslać[2], B. Frohnapfel[1]

1: Institute of Fluids Mechanics (ISTM), Karlsruhe Institute of Technology, Germany
2: LaVision GmbH, Anna-Vandenhoeck-Ring 19, 37081 Göttingen, Germany
*Corresponding author: jochen.kriegseis@kit.edu

Keywords: Turbulent channel flow, sublayer resolution, Lagrangian Particle Tracking (LPT), Shake-the-Box (STB)

ABSTRACT

Time-resolved Shake-the-Box (STB) experiments have been conducted in the channel-flow facility at the Institute of Fluid Mechanics (ISTM) at $f = 30\,\mathrm{kHz}$ repetition rate to study the near-wall velocity field at a viscous Reynolds number of $Re_\tau = 350$ (centerline velocity $U_\mathrm{cl} = 8.4\,\mathrm{m/s}$, channel half-height $h = 12.6\,\mathrm{mm}$, viscous unit $\delta_v \approx 36\,\mu\mathrm{m}$) to testify the STB method for the applicability to provide high-resolution velocity information of the given flow field including the sublayer region of the channel flow. In addition to the extraction of Lagrangian particle tracks and corresponding Eulerian iso-surfaces of vortical structure the major emphasis of the study centers around an evaluation of the resulting near wall velocity profile. Particularly, it is discussed how the choice of data-processing steps and strategies affects the resulting velocity estimates in the immediate vicinity of the wall, where the major impact for the current study has been identified to result from image-arithmetic efforts during data pre-processing. The achieved results are discussed and further compared with direct numerical simulations (DNS) of similar Re_τ and earlier experimental efforts at ISTM of the same flow configuration by means of stereoscopic particle image velocimetry (stereo PIV) and a laser-Doppler velocimetry profile sensor (LDV-PS). Finally, future perspectives of the experimental efforts for near-wall shear flow measurements are outlined on the grounds of the achieved insights.

1. Introduction

Well-resolved near-wall velocity measurements are an essential means for both a profound understanding and the evaluation of various flow-control strategies when applied to wall-bounded turbulent flows. In this context, particularly experimental investigations dealing with (fully-developed) turbulent channel flows build upon well-documented reference flows, such that an immediate comparison between this canonical base flow and the respectively considered actuation efforts becomes straight-forwardly possible.

Such experimental efforts, however, come with the challenge of limited spatial resolution in proximity of solid walls. Furthermore, this resolution issue becomes more prominent with increasing Reynolds numbers, due to the decreasing viscous length scale δ_v of the problem. Örlü & Vinuesa (2020) provide a comprehensive review of the variety of available direct and indirect methods for the estimation of wall-shear stress τ_w, where most of the latter, immediately rely on the accurate measurement of velocity in the sublayer region. Additional complexity comes into play, if plasma discharges are applied as means of active flow control (AFC), since arcing and other issues stemming from electromagnetic interference (EMI) render the application of e.g. thermal anemometry difficult (Benard & Moreau, 2014; Kotsonis, 2015).

One such plasma-based AFC experiment has been performed in a channel flow by Hehner et al. (2021), where the impact of virtual wall oscillations (Hehner et al., 2019) on the flow topology of the cross plane has been investigated by means of stereoscopic particle image velocimetry (stereo PIV) in the cross-plane of the flow. While the stereo PIV results clearly revealed the footprint of the AFC effort in the velocity fields, an immediate access to the viscous sublayer was not achieved due to resolution limits. This limit was explicitly addressed by Pasch et al. (2023), who investigated the applicability of laser Doppler velocimetry profile sensors (LDV-PS) in an attempt to identify a non-intrusive and EMI-resistant complementary means for recording the velocity information in the immediate vicinity of the channel walls.

The interplay of large-scale structures and the near-wall properties of the flow has been emphasized for the AFC approach of wall oscillations by Agostini & Leschziner (2018) and Marusic et al. (2021), for instance. Consequently, the simultaneous measurement of the spatio-temporally resolved velocity field from the viscous sublayer well into the boundary layer appears to be particularly beneficial in order to rigorously study the considered flow scenario. That is, the simultaneous availability of both the near-wall and bulk velocity fields are relevant to uncover the detailed local impact of the flow-control method and its global impact on the turbulent flow.

The overall spatio-temporal character of turbulent shear flows can be straight-forwardly studied by means of tomographic tracer-based flow measurement techniques (Raffel et al., 2018) such as tomographic particle image velocimetry (tomo-PIV, Scarano, 2013) and Lagrangian particle tracking (LPT, Schröder & Schanz, 2023). Furthermore, high-resolution LPT measurements with the Shake-the-Box (STB) method (Schanz et al., 2016) have also demonstrated good accuracy in the inner layer of a developing boundary layer in air (Schröder et al., 2015, 2018) and for channel-flow diagnostics in water (Abu Rowin & Ghaemi, 2019).

The purpose of the present study, therefore, centers around a comprehensive testification of the STB method for the applicability to provide high-resolution velocity information of the full flow field including the sublayer region of the channel flow facility as already used by Hehner et al. (2021) and Pasch et al. (2023). Note that the objective of this manuscript is twofold. As a first step implications of data-processing strategies on the resulting velocity profiles are compared. Additional emphasis subsequently lies on the comparison of the velocity profiles between STB (present study), LDV-PS (Pasch et al., 2023) and stereo PIV (Hehner et al., 2021) for similar friction Reynolds

numbers ($Re_\tau \approx 350$). Since the former aspect is still work in progress, the present manuscript does not yet provide convergence diagrams so as to evaluate the statistical significance of the results. Such efforts will follow in future investigations.

2. Experimental Procedure

2.1. Wind-tunnel facility and operating conditions

In continuation of the earlier tracer-based efforts by Hehner et al. (2021) and Pasch et al. (2023) the STB experiments are performed in the ISTM blower-type channel-flow facility. The test section has an overall length of $4000\,\mathrm{mm}$ and a cross-section aspect ratio of 12 spanning $300\,\mathrm{mm} \times 25.2\,\mathrm{mm}$ (width $\times$ height) to ensure fully developed channel-flow properties. The tunnel is operated at a bulk Reynolds number of $Re_b = 7.000$ based on the channel half height of $h = 12.6\,\mathrm{mm}$ and a center-line velocity of $U_{\mathrm{cl}} = 8.4\,\mathrm{m/s}$, which corresponds to a friction Reynolds number of $Re_\tau = 350$ and a viscous length scale of $\delta_v \approx 36\,\mu\mathrm{m}$.

Optical access for the measurement equipment is provided $100\,\mathrm{mm}$ upstream of the test-section outlet, where flush-mounted anti-reflection coated float glass windows ($1\,\mathrm{mm}$ thickness) are embedded into the top and side walls to ensure a high quality, low distortion optical access for cameras and laser sheet. Further details on the wind-tunnel facility can be found in the work of Hehner (2022).

2.2. Experimental set-up

The imaging set-up consists of four CMOS high-speed cameras (Phantom v1840, *Vision Research*, resolution: 2048 px $\times$ 1952 px, pixel pitch: $13.5\,\mu\mathrm{m}$, memory: $72\,\mathrm{GB}$), each equipped with a $100\,\mathrm{mm}$ macro lens (Milvus 2/100M, *Zeiss*) and a Scheimpflug adapter (Scheimpflug adapter v3, *LaVision*); see Figure 1. The cameras are placed in a pyramidial (*cross-like*, Scarano, 2013) configuration above the viewing window of the channel, resulting in camera angles between $39°$ and $54°$. The chosen optical magnification leads to an image scaling factor of 29.41 pixel/mm.

Volumetric illumination is provided by a dual-cavity high speed laser (DM2-100-532-DH, *Photonics Industries*, wavelength: $532\,\mathrm{nm}$, pulse energy: $10\,\mathrm{mJ}$ at $10\,\mathrm{kHz}$) and its emitted laser beam is introduced through a small window at the side of the channel. In order to achieve sharp edges of the illuminated volume, a set of apertures is placed in the laser-beam path to cut-out the low-energy tails of the laser beam. The lens apertures of the cameras in forward- and backward-scattering direction are set to $f\#$ = 9.5 and 6.7, respectively, to compensate for the varying scatter intensities. A common reconstruction volume of $\approx 15\,\mathrm{mm} \times 14\,\mathrm{mm} \times 4\,\mathrm{mm}$ is achieved this way.

The required seeding is provided by a Laskin-nozzle seeder (PIVPart40, *PIVTEC*), which atomizes the seeding fluid (PIVlight, *PIVTEC*) and produces droplets of $\approx 0.9\,\mu\mathrm{m}$ in diameter. Calibration of the multi-camera set-up is done utilizing a dual-level calibration plate (053-1-1, *LaVision*). The

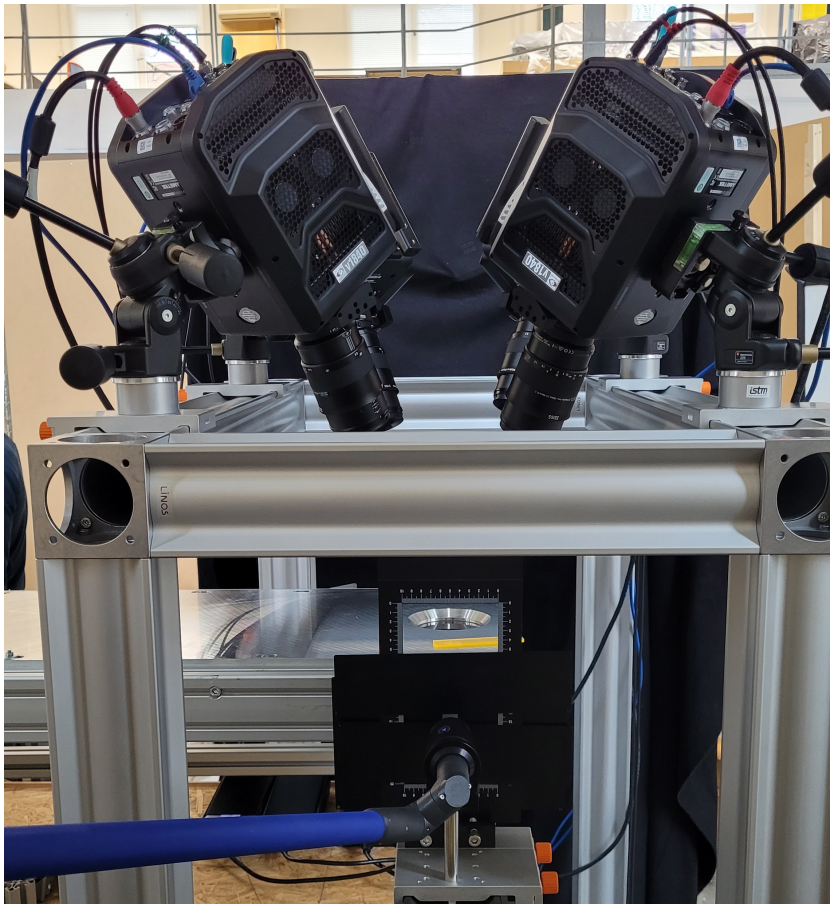

Figure 1. Photograph of the experimental set-up showing the four high-speed cameras in pyramidial configuration looking into the channel through a circular window and volumetric laser illumination through a window from the side (flow from left to right).

initial calibration error was on average 0.15 px across all cameras and has been further reduced well below 0.1 px after four volume-self calibration (VSC, Wieneke, 2008) iterations.

For optimal particle displacements in the range of 8-10 px an image acquisition frequency of $f = 30\,\mathrm{kHz}$ is utilized, which requires to crop the camera images to a resolution of 640 px $\times$ 304 px. According to the available camera memory a total number of 30.093 images is recorded corresponding to a measurement time of $1\,\mathrm{s}$. Note that ten consecutive repetitions of the identical experiment were performed for the sake of improved statistical significance and minimized measurement uncertainty resulting in a total number of 300.930 images for the tested friction Reynolds number $Re_\tau = 350$. However, only the first data set is evaluated and discussed in the present manuscript.

3. Data Processing and Results

From the recorded camera images, time-resolved three-dimensional particle tracks are reconstructed using the STB method (Schanz et al., 2016) method as implemented in DaVis 11 (*LaVision*). As the raw images show static background reflections and the particle images show effects of peak-

locking, pre-processing of these images seems necessary to optimally prepare them for the flow reconstruction. As such, the initial data-processing strategy included the removal of background reflections by subtracting the sliding minimum intensity image over five consecutive frames. Furthermore, light variations and intensity differences across the four cameras are homogenized by intensity normalization across all camera frames and across 300 px wide kernels. Note that this raw-image processing will be referred to as reference below during the course of processing variations.

For the optical transfer function (OTF, Schanz et al., 2013) calibration, the particle images should ideally represent a Gaussian shape. Therefore, a mild Gaussian smoothing (Gaussian with a kernel size of σ = 1.2 px) is applied to better condition the small particle images for the OTF calibration. Time-resolved STB reconstructions are performed for each recording separately with two-passes, i.e. processing all frames in forward- and backward-time direction.

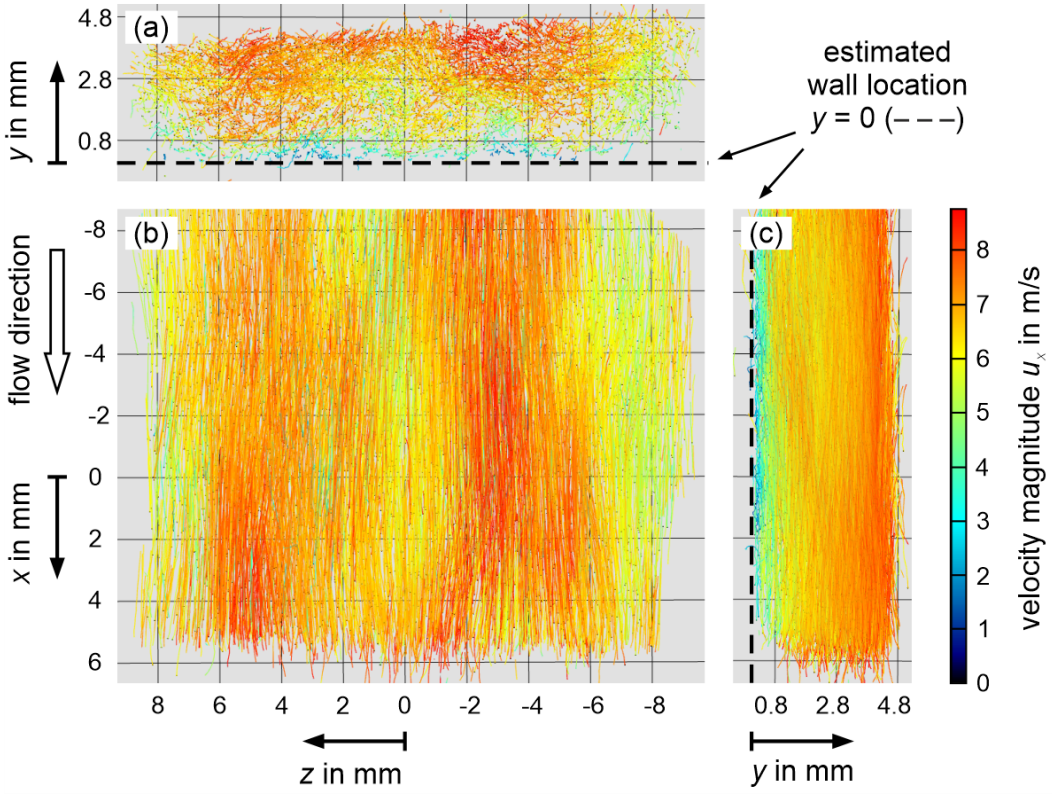

Figure 2. Instantaneous flow reconstruction results of the recorded flow field; (a) cross-plane view – bulk flow out of page, (b) wall-normal top-down view, (c) side view. Lagrangian particle trajectories drawn over 9 consecutive time steps, color-coded with respect to the velocity magnitude; identical color scale for all three diagrams.

3.1. Flow-field evaluation

Example reconstruction results are presented in Figure 2 and 3, which have been rearranged from the immediate DaVis11 export. The flow direction is towards positive x, and the wall-normal and spanwise coordinates are towards positive y and z, respectively. Note that only a preliminary

wall-location estimate $y \approx 0$ is included in the figures as dashed lines due to the known uncertainties of the wall-location determination (Örlü et al., 2010). This retroactive estimation effort and the resulting coordinate transformation into a wall-fixed frame of reference (x, y, z) will, however, follow below according to the treatise of Luchini (2018) during the course of the subsequent velocity-profile discussions.

Figure 2 shows approximately 4800 Lagrangian particle trajectories from different viewing directions; see Figure 2(a), 2(b) and 2(c). The tracks are color coded with respect to their velocity magnitude in order to indicate the presence of local fast-and slow-speed regions in the turbulent channel flow (identical color scale for all three diagrams). These clustered locations can also be directly identified from the cross-plane $(y - z)$ view in Figure 2(a), which indicate possible sweep and ejection events (see e.g. Devenport & Lowe, 2022). Furthermore, the varying track lengths in Figure 2(b) and 2(c) indicate the boundary-layer orientation via the staggered track lengths and approximate wall position.

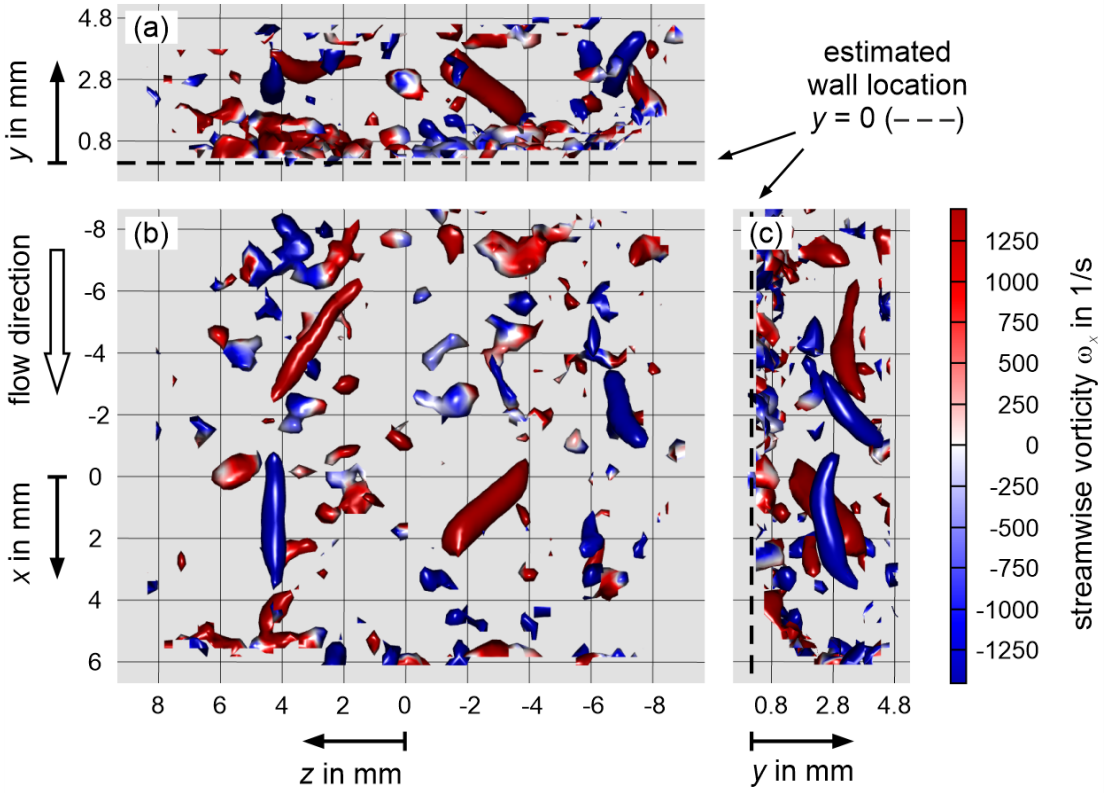

Figure 3. Instantaneous flow reconstruction results of the recorded flow field; (a) cross-plane view – bulk flow out of page, (b) wall-normal top-down view, (c) side view. Interpolated Eulerian flow field: Instantaneous vortical structures (iso-surfaces of the Q-criterion at $440\,000\,1/\mathrm{s}^2$, Hunt et al., 1988), color-coded by stream-wise vorticity; identical color scale for all three diagrams.

The interpolation of the Lagrangian tracks onto an Eulerian field is presented in Figure 3. Particularly, iso-surfaces of instantaneous vortical structures have been derived from a coarser interpolation of the particle trajectories onto a regular equidistant grid (bin size: 40 voxel, grid-spacing: $340\,\mu\mathrm{m}$) and are visualized via the Q-criterion at $440\,000\,1/\mathrm{s}^2$ (Hunt et al., 1988). To indicate the

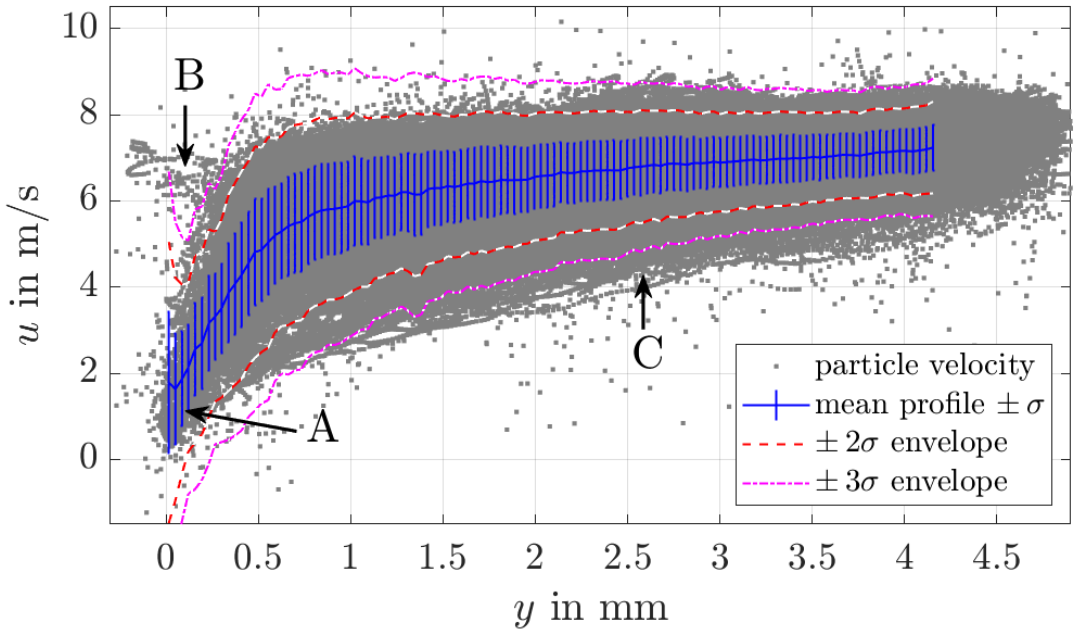

Figure 4. Ensemble averaged wall-normal profile $U(y)$ of the stream-wise velocity component $u(x, y, z, t)$ after binning of individual particle velocities in $48\,\mu\mathrm{m}$ sized y-bins. The standard deviation $\pm\sigma_u$ is indicated as vertical bars in the diagram; furthermore, additional envelopes of $\pm 2\sigma_u$ and $\pm 3\sigma_u$ are added for completeness.

sense of rotation, the surfaces are color-coded according to their streamwise vorticity component ω_x. Even though the outer rim of the recorded volume comprises several spurious small-scale structures near the wall and for $y > 3\,\mathrm{mm}$, the Eulerian reconstruction clearly reveals several quasi-streamwise vortices (Miyake et al., 1997).

3.2. Velocity-profile evaluation I: comparison of processing strategies

After STB, the particle tracks (for these presented results only from a subset of 100 time steps) are used to calculate a spatio-temporally averaged wall-normal profile $U(y)$ of the stream-wise velocity component $u(x, y, z, t)$ following the ideas of an ensemble binning as outlined by Agüera et al. (2016). The velocity values of the particles along the trajectories are deduced from a Savitzky-Golay filter (second-order, kernel size of 11 time steps, Savitzky & Golay, 1964). All reconstructed particles are then collected in bins of $36\,\mu\mathrm{m}$ size – i.e. one viscous length scale δ_v – over the entire reconstructed wall-normal distance of $4\,\mathrm{mm}$. Subsequently, the average stream-wise velocity component $U(y)$ is calculated as the mean value for all bins, which is further complemented by the determination of the bin-wise standard deviations (= root-mean-square values, rms) $\sigma_u(y) = u_{\mathrm{rms}}(y)$.

The obtained wall-normal velocity profile is presented in Figure 4. Within this figure, the mean profile $U(y)$ is plotted as the blue, solid line and the extend of the standard deviation $\pm\sigma_u(y)$ is marked by the vertical bars. All registered particle locations and velocities are embedded into the diagram as gray dots, which reveal the typical velocity-scatter distribution in the near-wall region

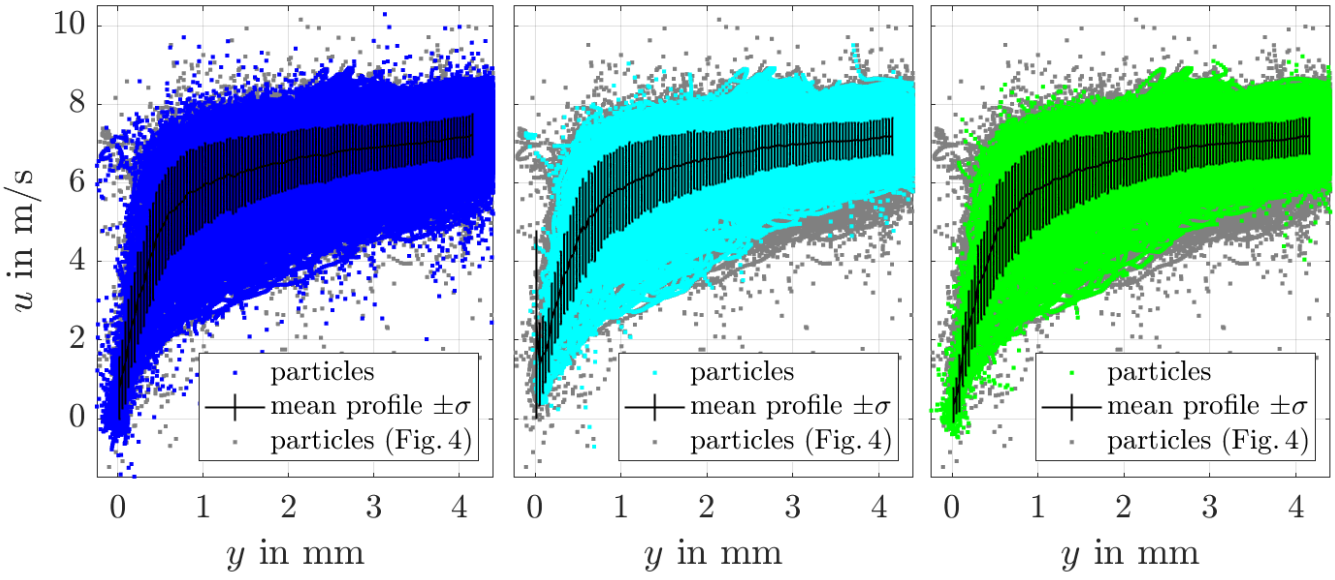

(a) omitted subtraction (b) rotation (c) no sub. & rot.

Figure 5. Influence of omitted sliding minimum subtraction and coordinate-system rotation on particle localization and velocity determination in comparison to the reference data of Figure 4; (a) omitted minimum subtraction reveals more slow particles in wall vicinity Figure 4, (b) coordinate-system rotation diminishes the presence of slower trajectories in the outer region of the boundary layer, (c) combination of both strategies reveals combined improvement.

of turbulent flows as outlined by Alfredsson et al. (2011). Furthermore, the coverage of twice and three times the standard deviation around the mean is indicated by the red dashed and magenta dash-potted lines as pre-cursor for the normalized probability density distribution (PDF) of the measurement results (cp. also Pasch et al., 2023). Even though Figure 4 already reasonably resembles the typical scatter distribution, various obvious flaws can be identified, which are labeled A, B and C in the diagram. Most intruding, the near-wall mean profile significantly overestimates the local velocity (A), which also leads to a substantial violation of the no-slip condition. The wall-proximity, furthermore, reveals several nonphysically fast particle tracks (B), which are attributed to the remaining presence of ghost particles. Finally, the lower edge of the particle cloud (C) appears to be significantly over-represented and also comprises substantial amounts of particles below the $u(y) - 3\sigma_u$ margin.

To study the impact of the afore-mentioned sliding minimum subtraction on the resulting near-wall particle detections, the subtraction step was omitted, which is shown in Figure 5(a) in comparison to the reference data of Figure 4. While the reference data lack from slow particles at the wall, the particle cloud of Figure 5(a) clearly comprises substantial amounts of particles in wall vicinity. Accordingly, the derived mean profile leads toward the no-slip condition at the wall. Likewise, the significantly incerased number of slow particles leads to a diminished effect of fast ghost particles (B), since the relative share of outliers is significantly reduced.

While A and B have been attributed to the image-processing step of the data-processing approach,

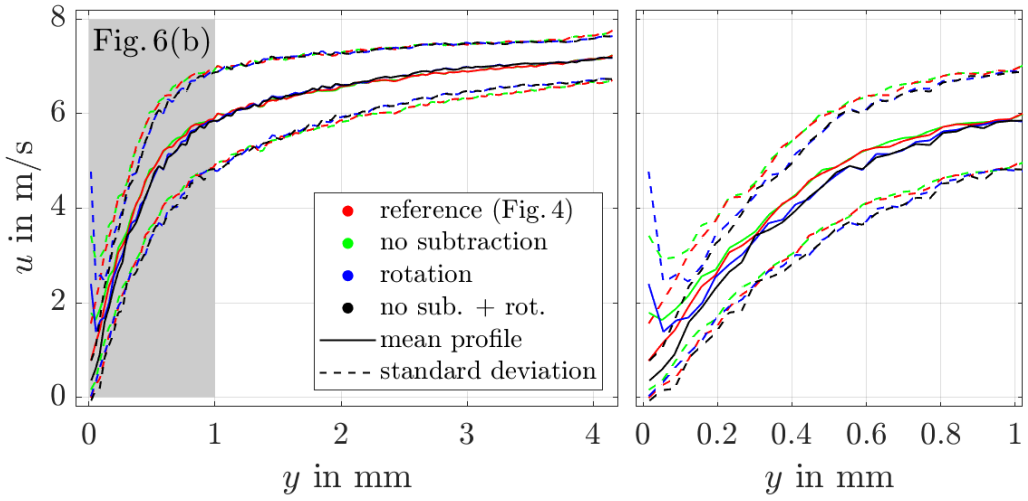

(a) comparison (b) zoomed view

Figure 6. Mean profiles and corresponding standard deviation of the comparative study of Figure 5.

C has been identified to result from minimal misalignment between the flow direction and the calibration target. Particularly, the mean profiles of wall-normal and spanwise velocity, $V(y)$ and $W(y)$ have been evaluated, where a non-zero remaining wall normal component $V(y > 1\,\mathrm{mm}) \approx 0.05\,\mathrm{m/s}$ has been found. To account for this minimal remaining misalignment of DaVis11-fixed frame of reference and the real flow direction, the coordinate system was rotated by

$$\alpha = \arctan\left(\overline{\frac{V(y > 1\,\mathrm{mm})}{U(y > 1\,\mathrm{mm})}}\right) \approx 0.7°. \tag{1}$$

Figure 5(b) shows the results of the such rotated coordinate system. In order to evaluate this effect isolated from the image processing optimizations, first the reference approach is considered. The comparison of the particle clouds saliently shows the reduced presence of slow particles in the C-labeled region of the data, while A and B appear not to be affected by this coordinate transformation. The combination of both optimization strategies is shown in Figure 5(c), which accordingly reveals either improvement.

A direct comparison of all applied processing strategies is provided in Figure 6. The effect of coordinate-system rotation can be identified in Figure 6(a), where the margin of standard deviation is diminished in the right half of the diagram for both rotated cases.

The influence of the data-processing modifications on the near-wall velocity profile is additionally displayed in Figure 6(b), which clearly shows the inflection points for both cases with sliding minimum subtraction. Furthermore, the comparison indicates that the pure rotation without omitted subtraction results in a deterioration of the resulting profiles. This result emphasizes the importance of a careful choice and combination of considered processing steps for the best-possible processing approach, which in the present case is the combination of both modifications. Consequently, only this case (i.e. no subtraction, rotation) will be considered in the next section.

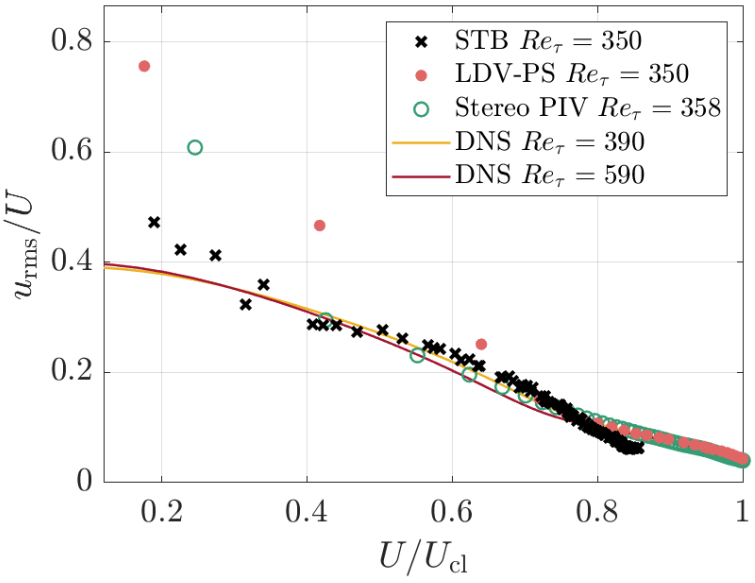

Figure 7. Diagnostic plot (adapted from Pasch et al., 2023) of the ensemble-averaged velocity profiles shown in Figure 5(c) together with reference DNS data at $Re_\tau = 390$ and 590 (Moser et al., 1999), LDV-PS data at $Re_\tau = 350$ (Pasch et al., 2023) and stereo PIV data at $Re_\tau = 358$ (Hehner et al., 2021).

3.3. Velocity-profile evaluation II: conversion into viscous units and comparison with literature

In an attempt to overcome the aforementioned uncertainties of wall-position estimation, Alfredsson & Örlü (2010) proposed the use of the so-called *diagnostic plot*, which plots the relative rms-velocity u_{rms}/U over the relative mean velocity U/U_{cl} under absence of any explicit location information. This implicit boundary-layer flow representation enjoys increasing attention and matured towards a robust means for the experimental diagnostics of wall-bounded turbulent flows (Alfredsson et al., 2021).

A diagnostic plot of the determined velocity data is shown in Figure 7, which display the results of the present STB measurements alongside the experimental tracer-based results from LDV-PS (Pasch et al., 2023) and stereo PIV (Hehner et al., 2021) measurements of similar friction Reynolds numbers. To provide further comparability to a DNS reference, the data of Moser et al. (1999) for $Re_\tau = 390$ and $Re_\tau = 590$ are added to the diagram.

Interestingly, the data of both imaging techniques (PIV and STB) similarly remain on the DNS curve towards significantly lower relative velocities U/U_{cl} as compared to the LDV-PS results, confirming the earlier insights of Pasch et al. (2023) with respect to the velocity-dependent uncertainty of particle location-estimations of the LDV-PS approach. Below $U/U_{\mathrm{cl}} < 0.4$ the results reveal gradually increasing rms-levels for the given velocity range, which indicate the increasing contribution of measurement uncertainty to the overall u_{rms} level towards the wall. Furthermore, the STB result drops below the DNS curve in the fastest margin of the recorded velocity field ($U/U_{\mathrm{cl}} > 0.75$). The diminished rms-level is likely to be related to an (as yet) unknown interrelation between focal depth, the occurrence of peak-locking effect and limited statistical significance of the evaluated

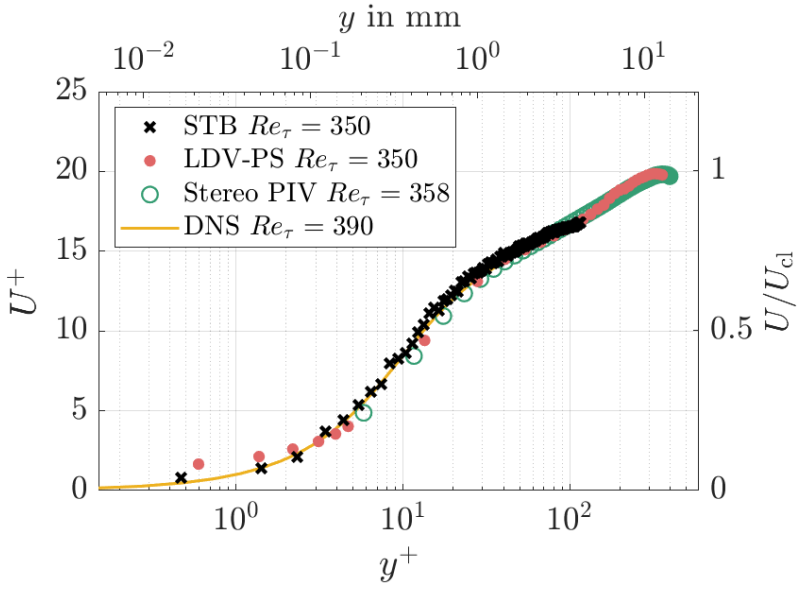

Figure 8. Ensemble-averaged velocity profiles of Figure 5(c) converted into viscous units (adapted from Pasch et al., 2023), plotted and compared with DNS data at $Re_\tau = 390$ (Moser et al., 1999) , LDV-PS data at $Re_\tau = 350$ (Pasch et al., 2023) and stereo PIV data at $Re_\tau = 358$ (Hehner et al., 2021). Additional physical coordinates appear on the upper and right axes, which refer to the current STB measurements at $Re_\tau = 350$.

data set. This observation consequently deserves further investigation so as to uncover its origin and corresponding consequences for the evaluation of turbulent boundary layers.

Finally, the achieved results are converted into dimensionless viscous (plus) units by means of the kinematic viscosity ν of the fluid and the friction velocity $u_\tau = \sqrt{\tau_w/\rho}$, where τ_w and ρ are the wall shear stress and fluid density, respectively. Note that τ_w and the wall location $y = 0$ have been determined retroactively via the general description of the dimensionless mean velocity profile by Luchini (2018) – similar to the reports by Hehner et al. (2021) and Pasch et al. (2023) of the same flow scenario.

The velocity profile of Figure 5(c) is accordingly converted into viscous velocity $U^+ = U/u_\tau$ and viscous (inner) wall distance $y^+ = yu_\tau/\nu = y/\delta_v$ and plotted in Figure 8. For orientation purposes also the physical y-coordinate and relative velocity U/U_{cl} are included as additional abscissa and ordinate, respectively. Similar to Figure 7 the results are displayed together with LDV-PS, PIV and DNS results of similar friction Reynolds number.

Obviously, the STB data reveal an overall agreement with the DNS reference and moreover span from $y^+ \propto \mathcal{O}(10^0)$ to $y^+ \propto \mathcal{O}(10^2)$. The relatively small slope of the STB data in the logarithmic regime might reflect the deviations in the diagnostic plot from reference data observed in this velocity regime. Based on the achieved plus-unit range the results already demonstrate the general applicability of the considered STB-approach for the desired simultaneous investigation of both viscous sublayer and logarithmic layer of the turbulent channel flow at reasonable spatial resolution. The result further suggest that channel flow at higher friction Reynolds numbers in the range

of $Re_\tau \propto \mathcal{O}(10^3)$ can be directly accessed with the present experimental/processing configuration, due to the fact that the bin-location of the first velocity information is at $y^+ = 0.39$ for the present case of $Re_\tau = 350$. Further resolution improvements (thus increasing researchable Re_τ-range with the present STB setup) is envisioned on the grounds of (i) bin-size reductions towards the direct evaluation of the immediate particle velocities and (ii) for reduced depths of the observed measurement volumes. Since the physical size of the logarithmic layer shrinks in physical size for increasing Re_τ, simultaneous flow field measurements as shown in Figure 2 and 3 up to the wake region of the velocity profile might remain possible.

4. Conclusions and Outlook

A time-resolved STB system has been applied and testified for its applicability for the characterization of turbulent channel flows. In continuation of earlier experimental studies by Pasch et al. (2023), this study contributes to the overarching goal to identify an experimental diagnostics approach – ideally comprised of only a single measurement technique – which might serve for an advanced evaluation metric for ongoing investigations into both active (Hehner et al., 2021) and furthermore also passive (von Deyn et al., 2022) flow control.

As expected from earlier STB-investigations (see. e.g. the review of Schröder & Schanz, 2023, on recent LPT advances), the recorded channel-flow data and derived LPT-information of the recorded particle images reveals a vast amount of particle trajectories, which have been directly converted into Eulerian data sets to allow the extraction of instantaneous velocity and vorticity fields. For the investigated test-section geometry ($h = 12.6\,\mathrm{mm}$) and friction Reynolds number $Re_\tau = 350$ reasonable results have been obtained.

Most importantly, the results indicate that the velocity profile in the sublayer region is reasonably well-resolved down to $y^+ < 1$, where this first proof-of-concept study already demonstrates competing resolution and accuracy as compared to the LDV-PS measurements of the same flow scenario by Pasch et al. (2023). This insight is encouraging news, as it renders the applied STB method a candidating approach to perform the desired simultaneous recording of both sublayer and loglayer information by means of a single measurement technique. As such, the STB-approach has been identified as particularly promising (single) measurement technique for an experimental investigation into turbulent channel flows, and moreover the quantitative spatio-temporal evaluation of influences stemming from respectively applied flow-control strategies.

As a technical note, the present proof-of-concept study also uncovered the complexity of the STB-approach to achieve physically meaningful data from the measurements. In the present case, the typically applied removal of background noise from the raw images erroneously also deleted the slowest range of particles from the images. In retrospect, the investigated flow scenario (i.e. high wall-normal gradients in proximity of a wall) appears too complex for this image-processing step, since the marginal particle displacement of < 1 pixel across the considered sliding raw-image average also interprets these particles as spurious noise. Omission of this processing step led to

encouraging results, i.e. a sufficient amount of meaningful particle detections for the determination of binned velocity profiles. However, in cases where the background subtraction remains mandatory for any reliable data evaluation, the POD-based image pre-processing as elaborated by Mendez et al. (2017) seems a promising candidate to fulfill either requirement, i.e. removal of background & preservation of particles.

A second processing issue has been identified as a quasi-hidden misalignment of $\approx 0.7°$ between processing coordinate system and real flow direction. Even though impossible to identify with the unaided eye, this minimal misalignment turned out to influence both the mean profile and standard deviations of the velocity profile $u(y)$. As demonstrated in this proof-of-concept study, potential issues arising from such misalignment can be easily erased by means of retro-active determination and subsequent correction between nominal and actual mean flow direction.

As a final remark, the insights achieved in this study outline a clear strategy towards the optimal data processing approach for the above mentioned large dataset of $10 \times 30.000 = 300.000$ time frames. Future efforts will, therefore, first further fine-tune the outlined processing strategies and then evaluate the large dataset with respect to the required (independent) sample number and duration for statistical significance and the correspondingly remaining uncertainty of the achieved results. On these ground also a thorough elaboration of the second-order moments beyond only σ_u will complement the evaluation of the obtained flow data.

Acknowledgements

This research is funded by the Deutsche Forschungsgemeinschaft (DFG, German Research Foundation) through project number 513183059 and the Struktur- und Innovationsfonds Baden-Württemberg (SI-BW, structural and innovation funds of Baden-Wuerttemberg).

References

Abu Rowin, W., & Ghaemi, S. (2019). Streamwise and spanwise slip over a superhydrophobic surface. *Journal of Fluid Mechanics*, *870*, 1127–1157. doi: 10.1017/jfm.2019.225

Agostini, L., & Leschziner, M. (2018). The impact of footprints of large-scale outer structures on the near-wall layer in the presence of drag-reducing spanwise wall motion. *Flow, Turbulence and Combustion*, *100*, 1037–1061. doi: 10.1007/s10494-018-9917-3

Agüera, N., Cafiero, G., Astarita, T., & Discetti, S. (2016). Ensemble 3D PTV for high resolution turbulent statistics. *Measurement Science and Technology*, *27*(12), 124011. doi: 10.1088/0957-0233/27/12/124011

Alfredsson, P. H., Örlü, R., & Schlatter, P. (2011). The viscous sublayer revisited–exploiting self-similarity to determine the wall position and friction velocity. *Experiments in Fluids*, *51*(1), 271–280. doi: 10.1007/s00348-011-1048-8

Alfredsson, P. H., Segalini, A., & Örlü, R. (2021). The diagnostic plot—a tutorial with a ten year perspective. In *Progress in Turbulence IX: Proceedings of the iTi Conference in Turbulence 2021 9* (pp. 125–135). doi: 10.1007/978-3-030-80716-0_17

Alfredsson, P. H., & Örlü, R. (2010). The diagnostic plot — a litmus test for wall bounded turbulence data. *European Journal of Mechanics - B/Fluids*, *29*(6), 403-406. doi: 10.1016/j.euromechflu.2010.07.006

Benard, N., & Moreau, E. (2014). Electrical and mechanical characteristics of surface ac dielectric barrier discharge plasma actuators applied to airflow control. *Experiments in Fluids*, *55*(11). doi: 10.1007/s00348-014-1846-x

Devenport, W. J., & Lowe, K. T. (2022). Equilibrium and non-equilibrium turbulent boundary layers. *Progress in Aerospace Sciences*, *131*, 100807. Retrieved from https://www.sciencedirect.com/science/article/pii/S0376042122000033 doi: https://doi.org/10.1016/j.paerosci.2022.100807

Hehner, M. T. (2022). *Dielectric-barrier discharge plasma actuators for turbulent friction-drag manipulation via spanwise oscillations* (Doctoral dissertation, Karlsruher Institut für Technologie (KIT)). doi: 10.5445/IR/1000155047

Hehner, M. T., Gatti, D., & Kriegseis, J. (2019). Stokes-layer formation under absence of moving parts – a novel oscillatory plasma actuator design for turbulent drag reduction. *Phys. Fluids*, *31*(5), 051701. doi: 10.1063/1.5094388

Hehner, M. T., Von Deyn, L. H., Serpieri, J., Pasch, S., Reinheimer, T., Gatti, D., … Kriegseis, J. (2021). Stereo piv measurements of oscillatory plasma forcing in the cross-plane of a channel flow. In *14th International Symposium on Particle Image Velocimetry*. Illinois Institute of Technology (Illinois Tech). doi: 10.18409/ispiv.v1i1.117

Hunt, J. C., Wray, A. A., & Moin, P. (1988). Eddies, streams, and convergence zones in turbulent flows. *Studying Turbulence Using Numerical Simulation Databases, 2. Proceedings of the 1988 Summer Program*, 193–208.

Kotsonis, M. (2015). Diagnostics for characterisation of plasma actuators. *Measurement Science and Technology*, *26*(9), 092001. doi: 10.1088/0957-0233/26/9/092001

Luchini, P. (2018). Structure and interpolation of the turbulent velocity profile in parallel flow. *European Journal of Mechanics - B/Fluids*, *71*, 15-34. doi: 10.1016/j.euromechflu.2018.03.006

Marusic, I., Chandran, D., Rouhi, A., Fu, M. K., Wine, D., Holloway, B., ... Smits, A. J. (2021). An energy-efficient pathway to turbulent drag reduction. *Nature Communications*, *12*(1), 5805. doi: 10.1038/s41467-021-26128-8

Mendez, M., Raiola, M., Masullo, A., Discetti, S., Ianiro, A., Theunissen, R., & Buchlin, J.-M. (2017). Pod-based background removal for particle image velocimetry. *Experimental Thermal and Fluid Science*, *80*, 181-192. Retrieved from https://www.sciencedirect.com/science/article/pii/S0894177716302266 doi: https://doi.org/10.1016/j.expthermflusci.2016.08.021

Miyake, Y., Ushiro, R., & Morikawa, T. (1997). The regeneration of quasi-streamwise vortices in the near-wall region. *JSME International Journal Series B*, *40*(2), 257-264. doi: 10.1299/jsmeb.40.257

Moser, R. D., Kim, J., & Mansour, N. N. (1999). Direct numerical simulation of turbulent channel flow up to $Re_\tau = 590$. *Physics of Fluids*, *11*(4), 943–945. doi: 10.1063/1.869966

Örlü, R., Fransson, J. H., & Alfredsson, P. (2010). On near wall measurements of wall bounded flows – the necessity of an accurate determination of the wall position. *Progress in Aerospace Sciences*, *46*(8), 353-387. doi: 10.1016/j.paerosci.2010.04.002

Örlü, R., & Vinuesa, R. (2020). Instantaneous wall-shear-stress measurements: advances and application to near-wall extreme events. *Measurement Science and Technology*, *31*(11), 112001. doi: 10.1088/1361-6501/aba06f

Pasch, S., Leister, R., Gatti, D., Örlü, R., Frohnapfel, B., & Kriegseis, J. (2023). Measurements in a turbulent channel flow by means of an ldv profile sensor. *Flow, Turbulence and Combustion*. doi: 10.1007/s10494-023-00469-4

Raffel, M., Willert, C. E., Scarano, F., Kähler, C. J., Wereley, S. T., & Kompenhans, J. (2018). 18. Applications: Volumetric flow measurements. In *Particle Image Velocimetry: A Practical Guide (3rd Edition)* (pp. 597–632). Cham: Springer International Publishing.

Savitzky, A., & Golay, M. J. E. (1964). Smoothing and differentiation of data by simplified least squares procedures. *Analytical Chemistry*, *36*(8), 1627-1639. doi: 10.1021/ac60214a047

Scarano, F. (2013). Tomographic piv: principles and practice. *Measurement Science and Technology*, *24*(1), 012001. doi: 10.1088/0957-0233/24/1/012001

Schanz, D., Gesemann, S., & Schröder, A. (2016). Shake-The-Box: Lagrangian particle tracking at high particle image densities. *Experiments in Fluids*, *57*(5), 70. doi: 10.1007/s00348-016-2157-1

Schanz, D., Gesemann, S., Schröder, A., Wieneke, B., & Novara, M. (2013). Non-uniform optical transfer functions in particle imaging: Calibration and application to tomographic reconstruction. *Measurement Science and Technology*, *24*(2), 024009. doi: 10.1088/0957-0233/24/2/024009

Schröder, A., & Schanz, D. (2023). 3D lagrangian particle tracking in fluid mechanics. *Annual Review of Fluid Mechanics*, *55*(1), 511-540. doi: 10.1146/annurev-fluid-031822-041721

Schröder, A., Schanz, D., Geisler, R., & Gesemann, S. (2018). 18.2. Near-wall turbulence characterization in a turbulent boundary layer using shake-the-box. In M. Raffel, C. E. Willert, F. Scarano, C. J. Kähler, S. T. Wereley, & J. Kompenhans (Eds.), *Particle Image Velocimetry: A Practical Guide (3rd Edition)* (pp. 600–605). Springer International Publishing.

Schröder, A., Schanz, D., Geisler, R., Novara, M., & Willert, C. (2015). Near-wall turbulence characterization using 4d-ptv "shake-the-box". In *11th International Symposium on Particle Image Velocimetry - PIV2015* (pp. 1–14).

von Deyn, L. H., Schmidt, M., Örlü, R., Stroh, A., Kriegseis, J., Böhm, B., & Frohnapfel, B. (2022). Ridge-type roughness: from turbulent channel flow to internal combustion engine. *Experiments in Fluids*, *63*(1), 18. doi: 10.1007/s00348-021-03353-x

Wieneke, B. (2008). Volume self-calibration for 3D particle image velocimetry. *Experiments in Fluids*, *45*, 549–556. doi: 10.1007/s00348-008-0521-5